Depletion layer dynamics of polyelectrolyte solutions under Poiseuille flow

Seong Jun Park[a], Anisha Shakya[a], and John T. King[a,1]

[a]Center for Soft and Living Matter, Institute for Basic Science, 44919 Ulsan, Republic of Korea

Edited by William R. Schowalter, Princeton University, Princeton, NJ, and approved July 10, 2019 (received for review January 13, 2019)

Complex liquids flow through channels faster than expected, an effect attributed to the formation of low-viscosity depletion layers at the boundaries. Characterization of depletion layer length scale, concentration, and dynamics has remained elusive due in large part to the lack of suitable real-space experimental techniques. The short length scales associated with depletion layers have traditionally prohibited direct imaging. By overcoming this limitation via adaptations of stimulated emission depletion (STED) microscopy, we directly measure the concentration profile of polymer solutions at a nonadsorbing wall under Poiseuille flow. Using this approach, we 1) confirm the theoretically predicted concentration profile governed by entropically driven depletion, 2) observe depletion layer narrowing at low to intermediate shear rates, and 3) report depletion layer composition that approaches pure solvent at unexpectedly low shear rates.

depletion layer dynamics | Poiseuille flow | superresolution microscopy

The physics of complex liquids at interfaces manifests in many practical and fundamental problems, such as flow of blood through vessels (1), transport across biological nanopores (2), and friction and lubrication of polymer brush fluids (3–5). One long-standing problem in fluid mechanics is the enhanced flow of polymer solutions under wall-bounded laminar flow (6–14). This observation, first made nearly a century ago, has been attributed to the formation of dynamic depletion layers (slip layers) (8, 12, 15), which are thin layers formed at the boundary where the polymer concentration is significantly lower than in the bulk solution. When simple liquids flow past a solid wall, the no-slip boundary condition prevents the motion of molecules immediately adjacent to the wall, generating drag on the overall flow and establishing a nonuniform flow front (16, 17). For polymer solutions under flow, the depletion layers relax the no-slip boundary condition and thus reduce drag on the bulk fluid (8, 12).

To date, most direct studies of depletion layers have been carried out under conditions where the distance between 2 walls (D) is on the order of or smaller than the polymer end-to-end distance ($\langle r^2\rangle^{1/2}$) (3, 13, 18–20). While flow under such conditions is of increasing interest due to the emergence of nanofluidics (2, 21), it represents a distinct regime of flow as the structure and dynamics of the fluid are inherently modified by such confinement (13, 22, 23). Studies of depletion layer dynamics under conditions where $D \gg \langle r^2\rangle^{1/2}$ are more scarce, mainly due to lack of experimental techniques capable of measuring nanoscale concentration profiles without directly perturbing the system (3, 18). Optical imaging has been applied for direct visualization of depletion layers of large polymers, such as xanthan (24) and DNA (25, 26). However, similar methods cannot be applied to systems in which the length scale associated with depletion layers is below the diffraction limit of light.

Here we study depletion layers of the polyelectrolyte poly(styrene sulfonate) (PSS; $N = 1{,}827$, $M_w = 334{,}400$, $M_w/M_n = 1.04$, 80% of monomer units negatively charged), at a nonadsorbing wall (fused silica), both at equilibrium and under Poiseuille flow, with distance between the walls $\sim 10^3 \cdot \langle r^2\rangle^{1/2}$. To spatially resolve the concentration profile of the polymer solution, we developed a technique based on stimulated emission depletion (STED) microscopy (27) coupled with pixel-by-pixel steady-state fluorescence anisotropy measurements. STED-anisotropy images reveal equilibrium depletion layers of PSS that closely follow the theoretically predicted concentration profile (28), with a decay length on the order of $\langle r^2\rangle^{1/2}$ of the polymer. Depletion layer dynamics under Poiseuille flow are quantified in terms of the Weissenberg number, $Wi = \dot{\gamma}\tau$, where $\dot{\gamma}$ is the shear rate and τ is the longest polymer relaxation time (29). The onset of depletion layer narrowing is observed at the critical Wi number ($Wi = 1$), which marks the flow rate at which the shear rate eclipses the polymer relaxation time, and thus, the polymer conformation begins to elongate (8). Within the range of $Wi = 1$ and $Wi = 10$, the thickness of the depletion layer decreases by a factor of 2. Furthermore, onset of changes in the polymer concentration of the depletion layer is well below the critical Wi, with the composition at the wall approaching that of pure solvent under the highest shear rates studied.

Results

Steady-State Fluorescence Anisotropy of Aqueous Polyelectrolyte Solutions. STED-anisotropy imaging developed for this study relies on imaging polymer concentration profiles in solution by contrasting spatially heterogeneous changes in the rotational dynamics of a small-molecule chromophore dispersed in the solution. By leveraging the interaction between AlexaFluor488 (water-soluble, net negative charge) and an anionic polymer (30, 31), local concentrations of the polymer can be estimated by steady-state anisotropy values (a). To calibrate the imaging protocol, we first measure bulk steady-state fluorescence anisotropy of deionized

Significance

The interfacial physics of complex liquids under flow remains a long-standing problem in fluid mechanics that is important for fields ranging from lubrication to nanofluidics. Liquids containing small amounts of high-molecular weight polymers are found to flow through channels faster than expected, a phenomenon attributed to the formation of boundary depletion layers that relaxes the no-slip boundary condition and allows the bulk of the fluid to slip past the walls. This work provides the most direct measurement to date of the dimension and composition of depletion layers of a polymer solution under flow. We anticipate extending this approach to help understand fluid dynamics in different regimes, such as flow in nanoconfinement and turbulence.

Author contributions: J.T.K. designed research; S.J.P. designed and built the microscope; S.J.P., A.S., and J.T.K. performed research; A.S. and J.T.K. analyzed data; and S.J.P., A.S., and J.T.K. wrote the paper.

The authors declare no conflict of interest.

This article is a PNAS Direct Submission.

[1]To whom correspondence may be addressed. Email: jtking@unist.ac.kr.

This article contains supporting information online at www.pnas.org/lookup/suppl/doi:10.1073/pnas.1900623116/-/DCSupplemental.

Published online July 31, 2019.

(DI) water solutions containing PSS and AlexaFluor488. PSS concentrations ranging from 0 to 40% wt/wt were used. Note that the maximum concentration tested for polymer solutions was $c^*/2$, where c^* is the overlap concentration of the polymer solution, so polymer chain entanglements are not expected to physically hinder chromophore rotation. The anisotropy value at each PSS concentration was calculated using

$$a = \frac{Int_{\parallel} - G \cdot Int_{\perp}}{Int_{\parallel} + 2G \cdot Int_{\perp}}, \quad [1]$$

where $Int_{\parallel}$ and $Int_{\perp}$ are the fluorescence intensities parallel and perpendicular to the excitation polarization, respectively, and G is a correction factor that accounts for depolarization induced by the optics of the instrument (32). G was calculated using AlexaFluor488 in DI water, assuming complete depolarization ($a = 0$).

The steady-state anisotropy values measured for AlexaFluor488 in PSS solutions (DI water) increase with increasing PSS concentration (Fig. 1, blue). This indicates a significant slowdown in the ensemble averaged rotational time constant of the chromophore. To further characterize the AlexaFluor488–PSS interactions, we perform dynamic anisotropy measurements (*SI Appendix*, section 1) which reveal 3 chromophore subpopulations: 1) free chromophores (unhindered rotation), 2) chromophores reversibly complexed with the polyelectrolyte (partially hindered rotation), and 3) chromophores irreversibly complexed with the polyelectrolyte (fully hindered rotation within the experimental timescales) (*SI Appendix*, Fig. S1). The contribution of each subpopulation to the steady-state anisotropy signal is dependent on the polyelectrolyte concentration (*SI Appendix*, Fig. S1 *C–E*). In addition, the fluorescence emission spectrum of AlexaFluor488 in PSS solution shows a red shift, the magnitude of the shift being dependent on PSS concentration (*SI Appendix*, section 2).

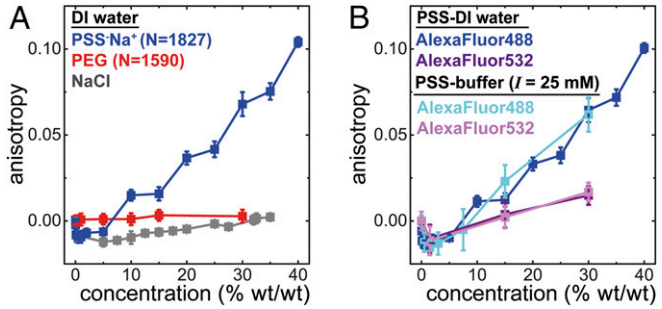

Fig. 1. Bulk steady-state fluorescence anisotropy of small-molecule chromophores in polymer solutions. (*A*) AlexaFluor488 in DI water solutions of PSS (blue), PEG (red), and NaCl only (gray). At [PSS] > 5% wt/wt, the anisotropy values increase significantly with increasing PSS concentration, indicating association of the chromophore with PSS. The initial decrease in anisotropy values at [PSS] < 5% wt/wt is due to the presence of Na^+ counterions in PSS solutions (see gray data markers for AlexaFluor488 in NaCl-only control). For PEG solutions, the anisotropy values are independent of PEG concentration over a comparable concentration range, as expected for noninteracting molecules. (*B*) Steady-state fluorescence anisotropy of AlexaFluor488 (blue and cyan) and AlexaFluo532 (purple and light pink) in PSS–DI water and PSS–buffer solutions (I = 25.0 mM) as a function of PSS concentration. In both DI water and buffer solutions, the increase in anisotropy values with increasing PSS concentration is comparable in magnitude. This shows that the chromophore interaction with PSS is independent of the ionic strength of the solution. Anisotropy values of AlexaFluor532 show a weaker dependence on PSS concentration compared with AlexaFluor488, as expected for chromophores having bulky side groups that disrupt short-range interactions.

The interaction between AlexaFluor488 and PSS can be attributed to short-range attraction between the anionic side group of the polymer and electron-depleted regions of the aromatic ring (33). These short-range interactions facilitate π-stacking of the chromophores (30, 31) that are independent of the solution ionic strength (34). Indeed, in both a Tris-EDTA buffer (buffer strength = 25 mM, ionic strength tuned to I = 25 mM using NaCl) and DI water, the steady-state anisotropy values increase comparably with increasing PSS concentration (Fig. 1 *B*, blue and cyan). Consistently, we find that the anisotropy values of the AlexaFluor532, a chromophore with steric side groups that disrupt short-range intermolecular stacking interactions between chromophores (31), are only weakly dependent on PSS concentration (Fig. 1 *B*, purple and light pink). Furthermore, in a control experiment with AlexaFluor488 in solutions of polyethylene glycol (PEG, N = 1,590) the anisotropy values are independent of PEG concentration (Fig. 1 *A*, red), as expected for noninteracting chromophore and polymer. Taken together, these results show that short-range interactions between the chromophore and the anionic side groups of the polyelectrolyte lead to hindered chromophore rotation resulting in an increase in the ensemble anisotropy values (30, 31).

Equilibrium Depletion Layer at a Nonadsorbing Wall. At equilibrium, a polymer solution forms a depletion layer driven by repulsions arising from a reduction in the configurational entropy (entropic repulsions) of the polymer as it approaches a nonadsorbing wall (35–37). As such, the thickness of the depletion layer (d) approximates $\langle r^2 \rangle^{1/2}$ of the polymer (37). The polymer concentration profile in the depletion layer, as a function of distance from the wall (x) (Fig. 2), follows the analytical function (28, 38)

$$\varphi(x) = \varphi_b \tanh^2\left(\frac{x}{d}\right) + \varphi_s, \quad [2]$$

where φ_b and φ_s are the bulk and surface concentration, respectively.

To probe the depletion layer of PSS at a nonadsorbing wall, we used a fused silica microfluidic channel (30 μm × 100 μm × 100 mm). A 10% solution of PSS in DI water (1 μM AlexaFluor488) was allowed to equilibrate for 30 min after injection into the channel. The PSS concentration is well below the overlap concentration ($c^*/6$); therefore, the solution is in an unentangled semidilute regime (39). Using a home-built STED-anisotropy microscope (*SI Appendix*, section 3) we image the anisotropy profiles extending from the wall to ∼1.50 μm into the bulk (Fig. 2*A*). Differences in fluorescence anisotropy values reflect differences in local polymer concentration (Fig. 2 *B* and *C*). A 2D STED-anisotropy image shows a pronounced decrease in average fluorescence anisotropy within a distance of few hundred nanometers from the wall (Fig. 2 *C*, *Top*). Averaging over the y dimension gives a 1D anisotropy profile characterized by the depletion layer thickness d, the anisotropy value at the wall ($a_{x=0}$), and the anisotropy value in the bulk solution (a_{bulk}) (Fig. 2 *C*, *Bottom*).

For PSS in DI water, the anisotropy value at the wall is smaller than that in bulk solution, which indicates depletion of polymer concentration near the wall (Fig. 2 *C* and *D*). The thickness of the depletion layer is measured to be 310 ± 42 nm (Fig. 2 *D*, gray). The PSS concentration at the wall is estimated to be ∼8% PSS wt/wt, which is only slightly lower than the bulk concentration (∼10% PSS wt/wt). The anisotropy profiles are well captured by Eq. **2** and hence provide a good estimate of polymer concentrations in the depletion layer. Note that the fluorescence intensity profile, which reflects only the spatial distribution of probe molecules, shows uniform signal near the wall (Fig. 2 *D*, *Inset*), indicating that the spatial profiles shown in Fig. 2*D* do not depend on the spatial distribution of the chromophore. Under the experimental conditions, the silica surface is expected to be

PHYSICS

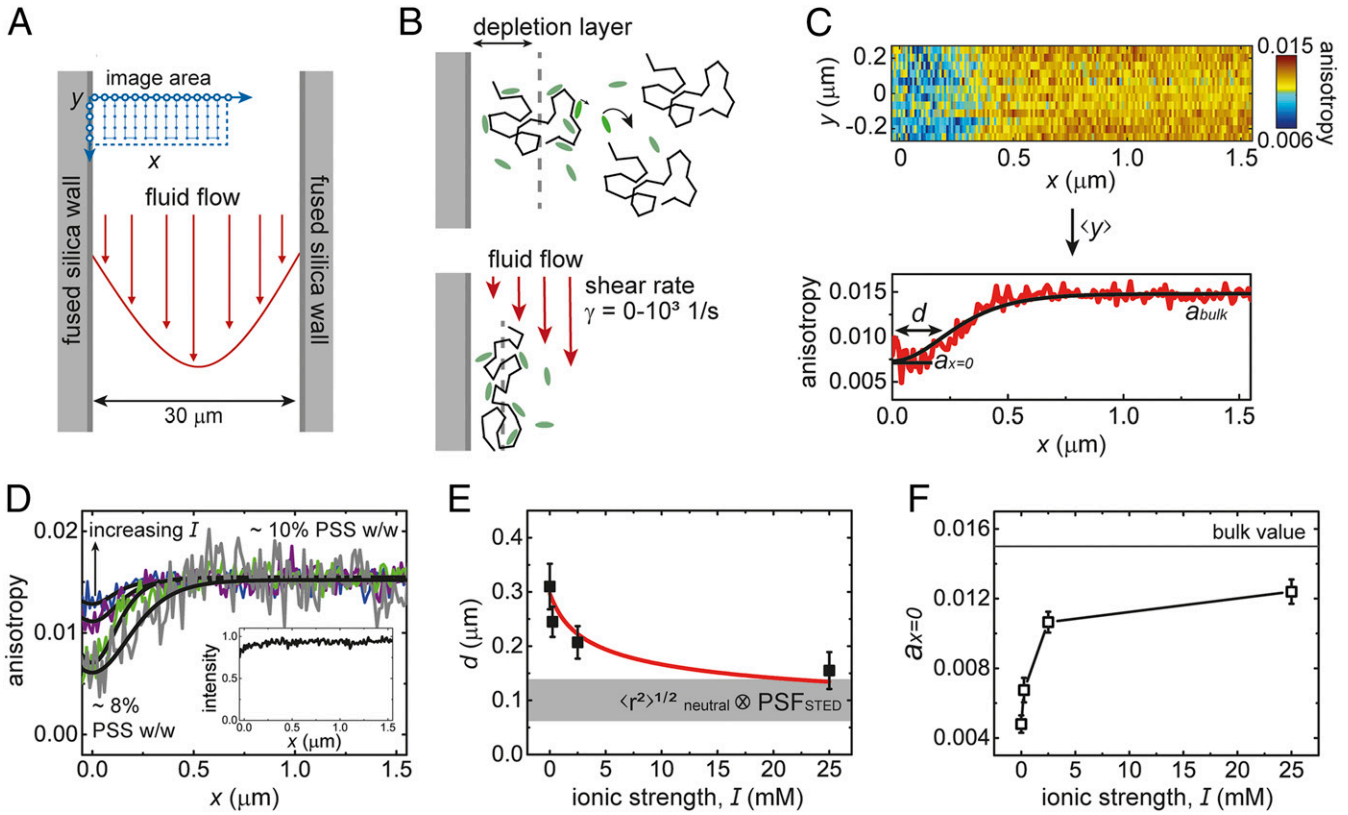

Fig. 2. Equilibrium depletion layers at nonadsorbing wall probed using STED-anisotropy imaging. (*A*) Cartoon of the experimental setup showing how the area of interest, with respect to the wall of the microfluidic device and the direction of fluid flow, is imaged. (*B*) Cartoon of depletion layer formation under equilibrium conditions (*Top*) and under shear induced by Poiseuille flow (*Bottom*). (*C*) Experimentally measured STED anisotropy image of PSS at a fused silica wall under conditions of no flow. The 1D anisotropy profiles are obtained by averaging over the *y* dimension of a 2D STED-anisotropy image. (*D*) Anisotropy profiles as a function of distance from the wall for PSS solutions varying in ionic strengths (DI water [gray], $I = 0.25$ mM [green], $I = 2.5$ mM [purple], and $I = 25$ mM [blue]) measured under conditions of no flow. *Inset* shows a representative fluorescence intensity profile indicating a uniform distribution of the chromophore. The anisotropy profiles are fit with Eq. **2** to obtain the depletion layer thickness (d) and PSS concentration at the wall ($a_{x=0}$). (*E*) d narrows with increasing ionic strength. The scaling of d with ionic strength is consistent with the scaling of $\langle r^2 \rangle^{1/2}$ (red curve) predicted from a WLC model (Eq. **3**). At high ionic strength, d approaches $\langle r^2 \rangle^{1/2}$ of the charge-neutral PSS chain convolved with the microscope PSF (gray box). (*F*) $a_{x=0}$ increases with increasing solution ionic strength indicating increased PSS concentration. The value plateaus below that of the bulk solution (gray line) at high ionic strengths, which confirms that depletion layers are formed under fully screened conditions.

negatively charged (40), although the electrostatic interaction length is estimated to be significantly less than 300 nm (*SI Appendix*, section 4).

Comparing the experimentally measured depletion layer thickness to $\langle r^2 \rangle^{1/2}$ of PSS in DI water is difficult as the highly charged nature of the PSS prevents direct calculation of the polymer size. However, the scaling of $\langle r^2 \rangle^{1/2}$ for a polyelectrolyte in solution as a function of ionic strength can be estimated using an appropriate model for polymer conformation and electrostatic persistence length. The wormlike chain (WLC) model is typically applied to semiflexible polyelectrolytes (41), such as PSS (42) and nucleic acids (43–45). We find that the experimental data are best captured by a WLC with an electrostatic persistence length given by Odijk–Skolnick–Fixman (OSF) theory (46, 47) (*SI Appendix*, section 5, for model comparisons). The $\langle r^2 \rangle^{1/2}$ can be estimated as

$$\langle r^2 \rangle^{1/2} \propto \left[\left(\frac{lL_p}{3} \right) - L_p^2 + \left(\frac{2L_p^3}{l} \right) - \left(\frac{2L_p^4}{l^2} \right) \cdot \left(1 - e^{l/L_p} \right) \right]^{1/2}, \quad [3]$$

where $l = Nb$ is the contour length, N is the number of monomers, b is the monomer length, and L_p is the persistence length of the polymer. According to OSF theory, the polyelectrolyte persistence length scales inversely with ionic strength. Therefore, with increasing solution ionic strength, due to reduced $\langle r^2 \rangle^{1/2}$, d is expected to narrow.

To characterize d with respect to $\langle r^2 \rangle^{1/2}$, we measured the depletion layer of PSS in Tris-EDTA buffer solutions at different ionic strengths. The buffer strength was varied from 25 to 0.25 mM. NaCl was added to the solution to tune the ionic strength of the buffer to the desired values (25.0, 2.50, and 0.25 mM final ionic strength of solution). We find that with increasing ionic strength, the depletion layer thickness decreases significantly (from $d = 310 \pm 42$ nm to $d = 127 \pm 25$ nm) (Fig. 2 *D* and *E*). The scaling of d with ionic strength obtained from experiments is in good agreement with the scaling of $\langle r^2 \rangle^{1/2}$ with ionic strength calculated using Eq. **3** (Fig. 2 *E*, red curve).

At high solution ionic strength, assuming the charges on the polymer backbone are fully screened, the $\langle r^2 \rangle^{1/2}$ of PSS can be calculated directly using the intrinsic persistence length of PSS ($\langle r^2 \rangle^{1/2} \sim 50$ nm) (48). Accounting for the point spread function (PSF) of the microscope, the experimentally measured value of d at highest ionic strength approaches the calculated $\langle r^2 \rangle^{1/2}$ (Fig. 2 *E*, gray box). The $a_{x=0}$ values are found to increase with increasing ionic strength (Fig. 2*F*), indicating increased polymer concentration in the depletion layer. This is expected as $\langle r^2 \rangle^{1/2}$ of

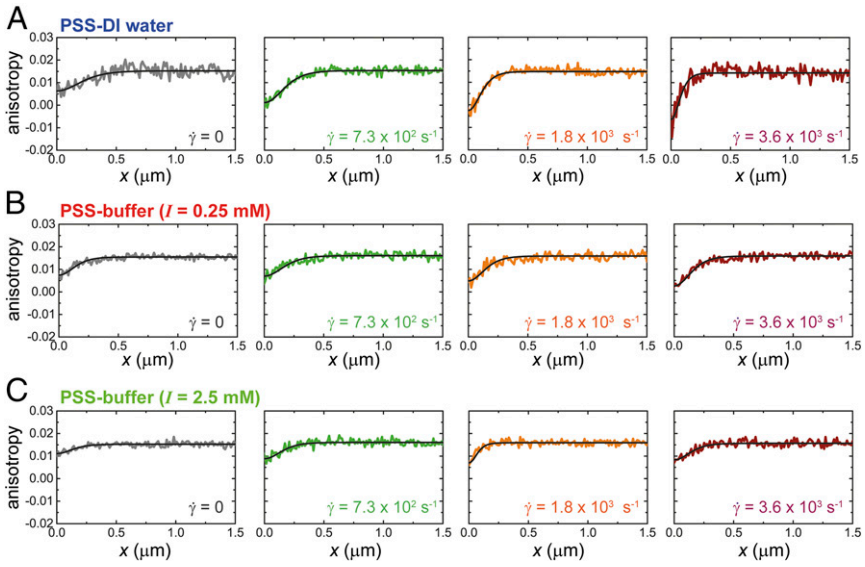

Fig. 3. Depletion layer dynamics under Poiseuille flow at nonadsorbing wall probed by STED-anisotropy imaging. Anisotropy profiles of PSS solutions in (*A*) DI water, (*B*) $I = 0.25$ mM, and (*C*) $I = 2.5$ mM at shear rates ranging from 0 to $3.6{\cdot}10^3$ s^{-1}. The anisotropy profiles are fit to Eq. **2** to obtain d and $a_{x=0}$ values.

the polymer decreases with increasing ionic strength due to chain collapse.

Depletion Layer Dynamics under Poiseuille Flow. Under Poiseuille flow, a shear force arises near the wall due to the no-slip boundary condition (Fig. 2*B*) (17). For polymer solutions, the shear elongates the chains in a direction parallel to the flow (10, 11, 13, 26, 49). While the dynamics of depletion layers under flow have been extensively studied via theory/modeling, the complete picture has not been confirmed experimentally. The most direct experimental study was by Ausserré et al. (50), who reported thickening of depletion layers in an aqueous solution of xanthan under flow at high shear rates. However, narrowing of depletion layers at low to intermediate shear rates, which has been theoretically predicted (11), has not been experimentally observed to date.

We probe depletion layers of PSS (10% wt/wt solution in DI water, 1 μM AlexaFluor488) under flow at intermediate shear rates (0 to $4{\cdot}10^3$ s^{-1}) (Fig. 3*A*). The Reynolds number under these conditions is <1 (*SI Appendix*, section 6), indicating that the flow is laminar (51). To compute *Wi*, we first calculate the relaxation time of PSS in DI water. For a polyelectrolyte solution in the unentangled semidilute regime the dynamics are expected to be Rouse-like (39),

$$\tau = \frac{\zeta b^2 N^2}{6\pi^2 k_B T p^2} \text{ for } p = 1,2,\ldots,N, \qquad [4]$$

where $p = 1$ gives the longest relaxation time. The friction coefficient (ζ) is given by Stokes' law ($\zeta = 6\pi\eta_s R_g$). The longest relaxation time for PSS in DI water is calculated to be $1.4{\cdot}10^{-3}$ s at room temperature, which yields a range of *Wi* from 0 to 10 (Fig. 4) for the shear rates employed in this study.

The depletion layer concentration profiles imaged by STED-anisotropy were fit to Eq. **2** (Fig. 3*A*). With increasing shear rate, 2 pronounced effects are observed: 1) depletion layer narrowing (decrease in depletion layer thickness as polymer center of mass approaches the wall) and 2) depletion layer sharpening (polymer concentration in the depletion layer approaches pure solvent) (Fig. 4). Note that in absence of polymer, no change in the anisotropy profile is observed with flow (*SI Appendix*, section 7).

Modeling studies suggest that depletion layer narrowing occurs due to shear-induced elongation and alignment of the polymer along the direction of flow (11, 52). Such deformation allows the center of mass of the polymer to approach the wall without incurring an entropic penalty. This mechanism is valid in the low to intermediate *Wi* regime ($Wi = 1 - 10$), where the average rotational time of the polymer is slower than the relaxation time of the deformation (11). At high *Wi*, where the average rotational time of the polymer is faster than its relaxation time (29), the depletion layers thicken as the effective time-averaged polymer size increases (11, 50).

The anisotropy profile as a function of distance from the wall sharpens with increasing shear (Fig. 4*B*). This observation, which reflects drifting of polymer segmental density away from the wall, can be attributed to the hydrodynamic lift generated by tension in the polymer chain induced by shear (13, 53–56). At the highest shear rate ($\dot{\gamma} \sim 7{\cdot}10^3 s^{-1}$) studied here, the polymer concentration measured at the wall approaches that of pure solvent (up to an order of magnitude lower than the bulk solution, <1% wt/wt).

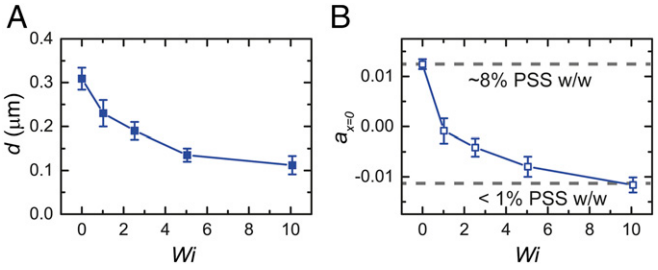

Fig. 4. Narrowing and sharpening of depletion layers at nonadsorbing wall under Poiseuille flow. (*A*) Depletion layer thickness (d) as a function of Weissenberg number (*Wi*) for PSS solutions in DI water. d narrows from ~310 to ~112 nm over a range of *Wi* from 0 to 10. (*B*) Polymer concentration at the wall ($a_{x=0}$) as a function of *Wi* for PSS solutions in DI water. At the highest shear rate studied here ($Wi \sim 10$), the polymer concentration in the depletion layer approaches pure solvent (~1 order of magnitude lower than that in bulk solution). Such depletion layer sharpening with increasing *Wi* is attributed to hydrodynamic lift pulling polymer segmental density away from the wall.

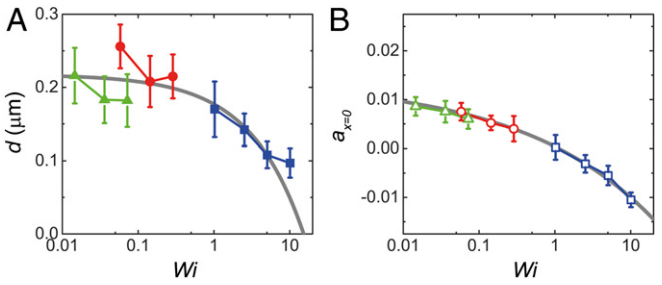

Fig. 5. Master plots of depletion layer thickness (d) and polymer concentration at the wall ($a_{x=0}$) for PSS solutions varying in ionic strengths (DI water [blue], I = 0.25 mM [red], and I = 2.5 mM [green]) as a function of Weissenberg number (Wi). The gray curves show power law fits to the data with scaling exponents of −0.40 and −0.25 for d and $a_{x=0}$, respectively. (*A*) Depletion layer narrowing onsets only above Wi = 1, where polymer chains begin to elongate due to shear. At high Wi the data deviate from the power law fit, likely indicating turnover from depletion layer narrowing to thickening that is expected at high shear rates. (*B*) Depletion layer sharpening is observed well below Wi = 1, suggesting that hydrodynamic lift can be generated without large-scale conformational changes to the polymer chains in the depletion layer.

Depletion Layer Dynamics at High Ionic Strength. In the previous sections, we show that the equilibrium depletion layer thickness approximates the $\langle r^2\rangle^{1/2}$ of a polyelectrolyte chain and decreases significantly with increasing solution ionic strength. We also report narrowing and sharpening of depletion layers at low to intermediate shear rates. In this section, we discuss the effect of flow on the polyelectrolyte depletion layers at high ionic strength.

PSS (10% wt/wt) in high-ionic strength buffer solutions (I = 0.25 and I = 2.5 mM, 1 μM AlexaFluor488) was subjected to shear rates of 0–4·10^3 s^{-1} (Fig. 3 *B* and *C*). The depletion layer concentration profiles imaged by STED-anisotropy were fit to Eq. **2** (Fig. 3 *B* and *C*). The presence of ions increases the internal relaxation time of the polymer, and therefore, Wi for each experimental condition must be calculated. For high-ionic strength solutions, the relaxation time was first estimated as (39)

$$\tau_{salt} = \tau \cdot (1 + 2Ac_s/c)^{-3/4}, \quad [5]$$

assuming that the solvent viscosity and Flory–Huggins interaction parameter are similar to the values in DI water. Here τ is the longest relaxation time in DI water, A is the average number of units between charges (based on 80% residues charged), c_s is the salt concentration, and c is the polymer concentration. The longest relaxation times of PSS at I = 0.25 mM and I = 2.5 mM are calculated to be 8·10^{-5} and 2·10^{-5} s, respectively.

Fig. 5 shows master plots of d and $a_{x=0}$ as a function of Wi (for PSS in DI water, I = 0.25 mM, and I = 2.5 mM), which fit to a power law with scaling factors of −0.40 and −0.25, respectively. The Wi numbers span 4 orders of magnitude from ∼10^{-2} to ∼10^1 across all ionic strength conditions used in this study. Below the critical Wi value (Wi = 1), no change in d is observed (Fig. 5*A*). However, significant narrowing of the depletion layer thickness sets in at the critical Wi. Over the range of Wi studied, d decreases from ∼310 to ∼112 nm. Note that at high Wi (∼10), d deviates from the power law fit, likely due to the turnover from depletion layer narrowing to thickening (11, 50).

Interestingly, depletion layer sharpening for the PSS solutions is observed below the critical Wi (Fig. 5*B*). This could arise from small perturbations to the local polymer structure (57). While these perturbations are too weak to modulate center of mass of the polymer, they could be sufficient to generate hydrodynamic lift at the wall (13, 53). This is reminiscent of Boger fluids (elastic polymer solutions that are engineered to prevent shear-induced elongation of the polymers), which show significant reductions in drag coefficients at $Wi \ll 1$ that plateau at the critical Wi (58).

Discussion

Superresolution anisotropy imaging employed in this study reveals depletion layer dynamics of polymer solutions, measured with a nonperturbative approach, at length scales previously inaccessible to traditional imaging techniques. We image depletion layers with thicknesses approximating the $\langle r^2\rangle^{1/2}$ of the polymer, in agreement with theoretical predictions for entropically driven depletion of polymer solutions at nonadsorbing walls (24, 28). We also report depletion layer narrowing under Poiseuille flow at low to intermediate shear rates. This drifting of the center of mass of the polymer in the depletion layer toward the wall is observed only above the critical Wi, where significant chain extension sets in. At higher Wi (∼10), the depletion layer thickness deviates from the observed trend, likely indicating a turnover to depletion layer thickening that has been predicted (11) and experimentally observed (24) at high Wi. Furthermore, measurements of concentration at the wall reveal significant segmental drift away from the wall (depletion layer sharpening) attributed to hydrodynamic lift. Unexpectedly, depletion layer sharpening is observed well below the critical Wi. This suggests that small perturbations to the polymer conformation can lead to sufficient chain tension to generate lift forces. Through real-space nanoscopic measurements, this work provides insights into the long-standing problem of enhanced flow of complex liquids.

Methods

Materials. Poly(styrene sulfonate) (M_w = 334,400, M_w/M_n = 1.04, N = 1,827, 80% charged) and poly(ethylene glycol) (M_w = 70,000, M_w/M_n = 1.28, N = 1,590, neutral) were purchased from Polymer Source. AlexaFluor488 and fluorescent polystyrene beads (100 nm) were purchased from Invitrogen, ThermoFisher. Fused silica microfluidic channels were purchased from Darwin Microfluidics.

Bulk Anisotropy Measurements. A steady-state spectrofluorimeter (Photon Technology International) equipped with linear polarizers (Thorlabs) in the excitation and emission pathways was employed for bulk anisotropy measurements. The excitation wavelength was set to 488 nm, and the detection wavelength was set to 510 nm.

STED-Anisotropy Imaging. A home-built setup was used for STED-anisotropy measurements. CW laser at 488 nm, generated by an OBIS LX 120 mW CW laser (Coherent), was passed through Glan–Taylor polarizer (Thorlabs) to obtain highly pure (100,000:1) linearly polarized excitation beam. CW laser at 592 nm (VFL-P-1000 592; MPB Communications Inc.) was passed through a vortex phase plate (VPP-1a; RPC Photonics) to generate a depletion with a doughnut profile. The excitation and depletion beams were focused on the sample using a 100×, 1.49 NA oil immersion objective (Nikon). Excitation modulation and synchronous detection were carried out according to *SI Appendix*, section 3.

The emitted fluorescence was collected by the same objective lens. The parallel and orthogonal components of the emitted fluorescence were separated by a polarizing cube (CCM1-PBS251; Thorlabs) and steered to 2 single-photon counters (SPCM-AQRH; EXCELITAS) for anisotropy measurements. The TTL signal from SPC was acquired with a DAQ card (PCIe-6353; National Instruments). Data acquisition and analysis was automated by custom LabVIEW software (National Instruments).

ACKNOWLEDGMENTS. We are grateful to the taxpayers who supported this work through the Korean Institute for Basic Science, project code IBS-R020-D1.

1. M. Abkarian, A. Viallat, Dynamics of vesicles in a wall-bounded shear flow. *Biophys. J.* **89**, 1055–1066 (2005).
2. D. Branton *et al.*, The potential and challenges of nanopore sequencing. *Nat. Biotechnol.* **26**, 1146–1153 (2008).
3. B. Bhushan, J. N. Israelachvili, U. Landman, Nanotribology—Friction, wear, and lubrication at the atomic-scale. *Nature* **374**, 607–616 (1995).
4. M. Chen, W. H. Briscoe, S. P. Armes, J. Klein, Lubrication at physiological pressures by polyzwitterionic brushes. *Science* **323**, 1698–1701 (2009).

5. J. Yu *et al*., Multivalent counterions diminish the lubricity of polyelectrolyte brushes. *Science* **360**, 1434–1438 (2018).
6. B. A. Toms, Detection of a wall effect in laminar flow of solutions of a linear polymer. *J. Colloid Sci.* **4**, 511–521 (1949).
7. R. G. Cox, S. G. Mason, Suspended particles in fluid flow through tubes. *Annu. Rev. Fluid Mech.* **3**, 291–316 (1971).
8. Y. Cohen, A. B. Metzner, Apparent slip-flow of polymer-solutions. *J. Rheol.* **29**, 67–102 (1985).
9. J. H. Aubert, M. Tirrell, Macromolecules in non-homogeneous velocity-gradient fields. *J. Chem. Phys.* **72**, 2694–2701 (1980).
10. E. Duering, Y. Rabin, Polymers in plane Poiseuille flow—Dynamic Monte-Carlo simulation. *J. Rheol.* **35**, 213–219 (1991).
11. J. J. Depablo, H. C. Ottinger, Y. Rabin, Hydrodynamic changes of the depletion layer of dilute polymer-solution near a wall. *AIChE J* **38**, 273–283 (1992).
12. U. S. Agarwal, A. Dutta, R. A. Mashelkar, Migration of macromolecules under flow—The physical origin and engineering implications. *Chem. Eng. Sci.* **49**, 1693–1717 (1994).
13. R. M. Jendrejack, D. C. Schwartz, J. J. de Pablo, M. D. Graham, Shear-induced migration in flowing polymer solutions: Simulation of long-chain deoxyribose nucleic acid in microchannels. *J. Chem. Phys.* **120**, 2513–2529 (2004).
14. M. D. Graham, Fluid dynamics of dissolved polymer molecules in confined geometries. *Annu. Rev. Fluid Mech.* **43**, 273–298 (2011).
15. H. A. Barnes, A review of the slip (wall depletion) of polymer-solutions, emulsions, and particle suspensions in viscometers—Its cause, character, and cure. *J. Nonnewton. Fluid Mech.* **56**, 221–251 (1995).
16. P. A. Thompson, S. M. Troian, A general boundary condition for liquid flow at solid surfaces. *Nature* **389**, 360–362 (1997).
17. E. Lauga, H. A. Stone, Effective slip in pressure-driven Stokes flow. *J. Fluid Mech.* **489**, 55–77 (2003).
18. A. J. Milling, Depletion and structuring of sodium poly(styrenesulfonate) at the silica-water interface. *J. Phys. Chem.* **100**, 8986–8993 (1996).
19. R. Khare, M. D. Graham, J. J. de Pablo, Cross-stream migration of flexible molecules in a nanochannel. *Phys. Rev. Lett.* **96**, 224505 (2006).
20. D. Stein, F. H. J. van der Heyden, W. J. A. Koopmans, C. Dekker, Pressure-driven transport of confined DNA polymers in fluidic channels. *Proc. Natl. Acad. Sci. U.S.A.* **103**, 15853–15858 (2006).
21. E. Secchi *et al*., Massive radius-dependent flow slippage in carbon nanotubes. *Nature* **537**, 210–213 (2016).
22. J. P. Gao, W. D. Luedtke, U. Landman, Layering transitions and dynamics of confined liquid films. *Phys. Rev. Lett.* **79**, 705 (1997).
23. J. Klein, E. Kumacheva, Confinement-induced phase transitions in simple liquids. *Science* **269**, 816–819 (1995).
24. C. Allain, D. Ausserre, F. Rondelez, Direct optical observation of interfacial depletion layers in polymer-solutions. *Phys. Rev. Lett.* **49**, 1694 (1982).
25. K. Jo, Y. L. Chen, J. J. de Pablo, D. C. Schwartz, Elongation and migration of single DNA molecules in microchannels using oscillatory shear flows. *Lab Chip* **9**, 2348–2355 (2009).
26. L. Fang, H. Hu, R. G. Larson, DNA configurations and concentration in shearing flow near a glass surface in a microchannel. *J. Rheol.* **49**, 127–138 (2005).
27. S. W. Hell, Far-field optical nanoscopy. *Science* **316**, 1153–1158 (2007).
28. J. F. Joanny, L. Leibler, P. G. de Gennes, Effects of polymer-solution on colloid stability. *J. Polym. Sci. B* **17**, 1073–1084 (1979).
29. C. M. Schroeder, R. E. Teixeira, E. S. G. Shaqfeh, S. Chu, Characteristic periodic motion of polymers in shear flow. *Phys. Rev. Lett.* **95**, 018301 (2005).
30. F. W. Morthland, P. P. H. De Bruyn, N. H. Smith, Spectrophotometric studies on the interaction of nucleic acids with aminoacridines and other basic dyes. *Exp. Cell Res.* **7**, 201–214 (1954).
31. D. F. Bradley, M. K. Wolf, Aggregation of dyes bound to polyanions. *Proc. Natl. Acad. Sci. U.S.A.* **45**, 944–952 (1959).
32. J. R. Lakowicz, *Principles of Fluorescence Spectroscopy* (Springer, Boston, MA, 2006).
33. B. L. Schottel, H. T. Chifotides, K. R. Dunbar, Anion-pi interactions. *Chem. Soc. Rev.* **37**, 68–83 (2008).
34. C. P. Brangwynne, P. Tompa, R. V. Pappu, Polymer physics of intracellular phase transitions. *Nat. Phys.* **11**, 899–904 (2015).
35. S. Asakura, F. Oosawa, On interaction between 2 bodies immersed in a solution of macromolecules. *J. Chem. Phys.* **22**, 1255–1256 (1954).
36. P. G. de Gennes, Conformations of polymers attached to an interface. *Macromolecules* **13**, 1069–1075 (1980).
37. P. G. de Gennes, Polymer-solutions near an interface. 1. Adsorption and depletion layers. *Macromolecules* **14**, 1637–1644 (1981).
38. R. R. Netz, D. Andelman, Neutral and charged polymers at interfaces. *Phys. Rep.* **380**, 1–95 (2003).
39. A. V. Dobrynin, R. H. Colby, M. Rubinstein, Scaling theory of polyelectrolyte solutions. *Macromolecules* **28**, 1859–1871 (1995).
40. S. H. Behrens, D. G. Grier, The charge of glass and silica surfaces. *J. Chem. Phys.* **115**, 6716–6721 (2001).
41. H. Yamakawa, W. H. Stockmayer, Statistical mechanics of wormlike chains. 2. Excluded volume effects. *J. Chem. Phys.* **57**, 2843–2854 (1972).
42. A. Brulet, F. Boue, J. P. Cotton, About the experimental determination of the persistence length of wormlike chains of polystyrene. *J. Phys. II* **6**, 885–891 (1996).
43. H. Chen *et al*., Ionic strength-dependent persistence lengths of single-stranded RNA and DNA. *Proc. Natl. Acad. Sci. U.S.A.* **109**, 799–804 (2012).
44. D. R. Jacobson, D. B. McIntosh, M. J. Stevens, M. Rubinstein, O. A. Saleh, Single-stranded nucleic acid elasticity arises from internal electrostatic tension. *Proc. Natl. Acad. Sci. U.S.A.* **114**, 5095–5100 (2017).
45. A. Y. L. Sim, J. Lipfert, D. Herschlag, S. Doniach, Salt dependence of the radius of gyration and flexibility of single-stranded DNA in solution probed by small-angle x-ray scattering. *Phys. Rev. E Stat. Nonlin. Soft Matter Phys.* **86**, 021901 (2012).
46. T. Odijk, Polyelectrolytes near the rod limit. *J. Polym. Sci. B* **15**, 477–483 (1977).
47. J. Skolnick, M. Fixman, Electrostatic persistence length of a wormlike polyelectrolyte. *Macromolecules* **10**, 944–948 (1977).
48. E. Hirose, Y. Iwamoto, T. Norisuye, Chain stiffness and excluded-volume effects in sodium poly(styrenesulfonate) solutions at high ionic strength. *Macromolecules* **32**, 8629–8634 (1999).
49. R. M. Jendrejack, E. T. Dimalanta, D. C. Schwartz, M. D. Graham, J. J. de Pablo, DNA dynamics in a microchannel. *Phys. Rev. Lett.* **91**, 038102 2003).
50. D. Ausserre, J. Edwards, J. Lecourtier, H. Hervet, F. Rondelez, Hydrodynamic thickening of depletion layers in colloidal solutions. *Europhys. Lett.* **14**, 33–38 (1991).
51. A. D. Stroock *et al*., Chaotic mixer for microchannels. *Science* **295**, 647–651 (2002).
52. C. M. White, M. G. Mungal, Mechanics and prediction of turbulent drag reduction with polymer additives. *Annu. Rev. Fluid Mech.* **40**, 235–256 (2008).
53. H. B. Ma, M. D. Graham, Theory of shear-induced migration in dilute polymer solutions near solid boundaries. *Phys. Fluids* **17**, 083103 (2005).
54. C. Sendner, R. R. Netz, Hydrodynamic lift of a moving nano-rod at a wall. *Europhys. Lett.* **79**, 58004 (2007).
55. C. Sendner, R. R. Netz, Shear-induced repulsion of a semiflexible polymer from a wall. *Europhys. Lett.* **81**, 54006 (2008).
56. L. G. Leal, Particle motions in a viscous-fluid. *Annu. Rev. Fluid Mech.* **12**, 435–476 (1980).
57. I. S. Dalal, N. Hoda, R. G. Larson, Multiple regimes of deformation in shearing flow of isolated polymers. *J. Rheol.* **56**, 305–332 (2012).
58. R. P. Chhabra, P. H. T. Uhlherr, D. V. Boger, Influence of fluid elasticity on the drag coefficient for creeping flow around a sphere. *J. Nonnewton. Fluid Mech.* **6**, 187–199 (1980).